European Journal of Mechanics / A Solids 73 (2019) 126–136

Contents lists available at ScienceDirect

European Journal of Mechanics / A Solids

journal homepage: www.elsevier.com/locate/ejmsol

Microscopic instabilities and elastic wave propagation in finitely deformed laminates with compressible hyperelastic phases

Jian Li[a], Viacheslav Slesarenko[a], Stephan Rudykh[b,*]

[a] Department of Aerospace Engineering, Technion – Israel Institute of Technology, Haifa, 32000, Israel
[b] Department of Mechanical Engineering, University of Wisconsin – Madison, Madison, WI53706, United States

ARTICLE INFO

Keywords:
Layered composite
Compressibility
Instability
Band gap
Postbuckling
Wave propagation

ABSTRACT

In this paper, we study the elastic instability and wave propagation in compressible layered composites undergoing large deformations. We specifically focus on the role of compressibility on the onset of instability, and elastic wave band gaps (forbidden frequency ranges) in finitely deformed buckled laminates. We employ the Bloch-Floquet analysis to study the influence of compressibility on the onset of instability and the corresponding critical wavelengths. Then, the obtained information about the critical wavelengths is used in the subsequent numerical postbuckling simulations. By application of the Bloch wave numerical analysis implemented in the finite element code, we investigate the elastic wave band gaps of buckled layered composites with compressible phases.

The compressible laminates require larger strains to trigger mechanical instabilities. This results in lower amplitudes of instability induced wavy patterns in compressible laminates as compared to incompressible layered materials. The instability induced wavy patterns give rise to tunability of the widths and locations of shear wave band gaps (that are not tunable by deformation in LCs with neo-Hookean phases in the stable regime); this tunability, however, is not significant in comparison to the tunability of the pressure wave band gaps. Thus, the complete band gaps (frequency ranges where neither shear nor pressure wave can propagate) can be controlled by deformation in both stable and post-buckling regimes.

1. Introduction

Design of microstructured metamaterials for manipulating elastic wave propagation has drawn considerable attention (Babaee et al., 2016; Bigoni et al., 2013; Celli et al., 2017; Celli and Gonella, 2015; Chen and Elbanna, 2016; Chen and Wang, 2016; Harne and Urbanek, 2017; Matlack et al., 2016; Miniaci et al., 2016; Srivastava, 2016; Trainiti et al., 2016; Xu et al., 2015; Zhu et al., 2014; Zigoneanu et al., 2014). These new materials can potentially serve for enabling various applications, such as wave guide (Casadei et al., 2012), vibration damper (Javid et al., 2016), cloaking (Zhang et al., 2011), and subwavelength imaging (Wood et al., 2006; Zhu et al., 2011). Recently, soft metamaterials with reconfigurable microstructures in response to external stimuli, such as mechanical load (dell'Isola et al., 2016; Galich et al., 2017a; Li et al., 2016; Meaud and Che, 2017; Zhang and Parnell, 2017), electric and/or magnetic field (Bayat and Gordaninejad, 2015; Galich and Rudykh, 2017, 2016; Gei et al., 2011; Huang et al., 2014; Jandron and Henann, 2017; Yang and Chen, 2008), attracted significant interest for tuning elastic wave propagation. Moreover, the elastic instability induced buckling phenomena, giving rise to a sudden change in microstructure, have been demonstrated to be greatly instrumental for the design of switchable phononic crystals. Thus, Bertoldi and Boyce (2008a, 2008b) introduced the concept of instability assisted elastic wave band gaps (BGs) control in soft elastomeric materials with peridically distributed circular voids (Shan et al., 2014; Wang et al., 2014, 2013). Rudykh and Boyce (2014) showed that the elastic instability induced wrinkling of interfacial layers could be utilized to control the BGs in deformable layered composites (LCs). In this work, we analyze the phenomena with specific focus on the influence of the constituent compressibility on the instabilities and elastic wave BGs of finitely deformed neo-Hookean laminates in the postbuckling regime.

The important work on the stability of layered and fiber composites by Rosen (1965), considered stiff layers embedded in a soft matrix as elastic beams on an elastic foundation, and derived an explicit expression to predict the critical buckling strain. Parnes and Chiskis (2002) revisited the instability analysis in linear elastic LCs, and they found that the buckling strain of dilute composites that experienced microscopic instability was constant, while for the macroscopic case,

* Corresponding author.
E-mail address: rudykh@wisc.edu (S. Rudykh).

https://doi.org/10.1016/j.euromechsol.2018.07.004
Received 19 November 2017; Received in revised form 5 July 2018; Accepted 9 July 2018
Available online 20 July 2018
0997-7538/

the buckling strain agreed with the results of Rosen (1965). Triantafyllidis and Maker (1985) analyzed the onset of instability in finitely deformed periodic layered composites. They demonstrated the existence of the microscopic and macroscopic (or long wave) instabilities by employing the Bloch-Floquet analysis (Geymonat et al., 1993), along with the loss of ellipticity analysis that is typically used to detect the onset of macroscopic instability (Merodio and Ogden, 2005, 2003, 2002). Nestorovic and Triantafyllidis (2004) investigated the interplay between macroscopic and microscopic instability of hyperelastic layered media subjected to combinations of shear and compression deformation. Micromechanics based homogenization was utilized to predict the macroscopic instability of transversely isotropic fiber composites with hyperelastic phases (Agoras et al., 2009; Rudykh and Debotton, 2012). Recently, Gao and Li (2017) showed that the wavy patterns of the interfacial layer could be tuned by the interphase between the interfacial layer and soft matrix. Slesarenko and Rudykh (2017) implemented the Bloch-Floquet technique into the finite element based code and examined the macroscopic and microscopic instability of periodic hyperelastic 3D fiber composites. More recently, Galich et al. (2018) focused on the influence of the periodic fiber distribution on instabilities and shear wave propagation in the hyperelastic 3D fiber composites. Furthermore, the microscopic and macroscopic instability phenomena of multi-layered composites under plane strain conditions were observed in experiments via 3D-printed layered materials (Li et al., 2013). Slesarenko and Rudykh (2016) experimentally showed that the wavy patterns in LCs with visco-hyperelastic constitutes could be tuned by the applied strain rate. Li et al. (2018a) experimentally realized the instability development in periodic 3D fiber composites. Through these studies, the role of stiff fiber reinforcement on the stability of composites has been well understood; in particular, the composites with stronger reinforcement (with higher shear modulus contrasts or with larger fiber volume fractions) are more prone to instabilities. However, the role of phase compressibility on the instability development and post-buckling behavior of hyperelastic laminates has not been examined.

In the first part of our paper, we will focus on the influence of phase compressibility on the onset of instability and critical wavelengths that define the postbuckling patterns of the microstructure. We note that it is possible to use the estimates for the onset of instability and critical wavelengths based on the linear elasticity theory (Li et al., 2013; Rudykh and Boyce, 2014); this, however, does not fully account for the nonlinear effects of finite deformations. To take into account these effects, we perform the instability analysis superimposed on finite deformations. The obtained information about the critical wavelengths is further used in the analysis presented in the second part of the paper, where the elastic waves in the postbuckling regime are analyzed.

Rytov (1956) derived explicit dispersion relations for elastic waves propagating perpendicular to the layers showing the existence of the elastic wave BGs (or stop bands) in LC frequency spectrum. Wu et al. (2009), and Fomenko et al. (2014) investigated the elastic wave BGs of layered media with functionally graded materials. Recently, Srivastava (2016) predicted the appearance of negative refraction at the interface between layered composite media and homogeneous material. More recently, Slesarenko et al. (2018) showed that negative group velocity can be induced by deformation in hyperelastic composites in the stable regime near elastic instabilities. Galich et al. (2017a) obtained explicit expressions for shear and pressure long waves in finitely deformed LCs with isotropic hyperelastic phases. Moreover, based on the analysis by Rytov (1956), Galich et al. (2017a) extended the classical results to the class of finitely deformed hyperelastic laminates. In particular, Galich et al. (2017a) show that the shear wave BGs are independent of the applied deformation in neo-Hookean laminates. In addition, the results of Galich et al. (2017a) demonstrate that the pressure wave BGs can be tuned by deformation, mostly via the change in the thickness of the layers. In this work, we examine the elastic wave propagation in finitely deformed neo-Hookean laminates in the *postbuckling* regime, and we specifically focus on the influence of material compressibility.

The paper is structured as follows: Section 2 presents the theoretical background for finite elastic deformation and small amplitude motions superimposed on the finitely deformed state. The numerical simulations, including the procedures to detect the onset of instability and perform postbuckling analysis, are described in Section 3. The results are presented in Section 4, which is divided into two subsections. Section 4.1 is devoted to the analysis of the influence of the constituent compressibility on the onset of instability; and Section 4.2 presents the analysis of elastic wave propagation in finitely deformed compressible LCs in the postbuckling regime. Section 5 concludes the study with a summary and discussion.

2. Theoretical background

Consider a continuum body and identify each point in the undeformed configuration with its position vector $\mathbf{X}$. When the body is deformed, the new location of the corresponding point is defined by mapping function $\mathbf{x} = \boldsymbol{\chi}(\mathbf{X}, t)$. The deformation gradient is defined by $\mathbf{F} = \partial\mathbf{x}/\partial\mathbf{X}$ and its determinant is $J = \det(\mathbf{F}) > 0$. For hyperelastic materials whose constitutive behaviors are described in terms of strain energy density function $W(\mathbf{F})$, the first Piola-Kirchhoff stress tensor is given by

$$\mathbf{P} = \frac{\partial W(\mathbf{F})}{\partial \mathbf{F}}. \tag{1}$$

In the absence of body forces, the equations of motion can be written in the undeformed configuration as

$$\mathrm{Div}\,\mathbf{P} = \rho_0 \frac{D^2\boldsymbol{\chi}}{Dt^2}, \tag{2}$$

where Div(•) represents the divergence operator in the undeformed configuration, $D(\bullet)/Dt$ is the material time derivative, and ρ_0 denotes the initial material density. When deformation is applied quasi-statically, Eq. (2) reads

$$\mathrm{Div}\,\mathbf{P} = 0. \tag{3}$$

Next we consider small amplitude motions superimposed on an equilibrium state (Destrade and Ogden, 2011; Ogden, 1997). The equations of the incremental motion are

$$\mathrm{Div}\,\dot{\mathbf{P}} = \rho_0 \frac{D^2\mathbf{u}}{Dt^2}, \tag{4}$$

where $\dot{\mathbf{P}}$ is an incremental change in the first Piola-Kirchhoff stress tensor and $\mathbf{u}$ is an incremental displacement. The incremental change in deformation gradient is given by

$$\dot{\mathbf{F}} = \mathrm{Grad}\,\mathbf{u}, \tag{5}$$

where Grad (•) represents the gradient operator in the undeformed configuration.

The linearized constitutive law can be expressed as

$$\dot{P}_{ij} = \mathscr{A}_{0ijkl}\dot{F}_{kl}, \tag{6}$$

where $\mathscr{A}_{0ijkl} = \partial^2 W/\partial F_{ij}\partial F_{kl}$ is the tensor of elastic modulus. Substitution of Eqs. (5) and (6) into Eq. (4) yields

$$\mathscr{A}_{0ijkl}\frac{\partial^2 u_k}{\partial X_j \partial X_l} = \rho_0 \frac{D^2 u_i}{Dt^2}. \tag{7}$$

In the updated Lagrangian formulation, Eq. (7) reads

$$\mathscr{A}_{ijkl}\frac{\partial^2 u_k}{\partial x_j \partial x_l} = \rho \frac{\partial^2 u_i}{\partial t^2}, \tag{8}$$

where $\mathscr{A}_{ipkq} = J^{-1}\mathscr{A}_{0ijkl}F_{pj}F_{ql}$ and $\rho = J^{-1}\rho_0$.

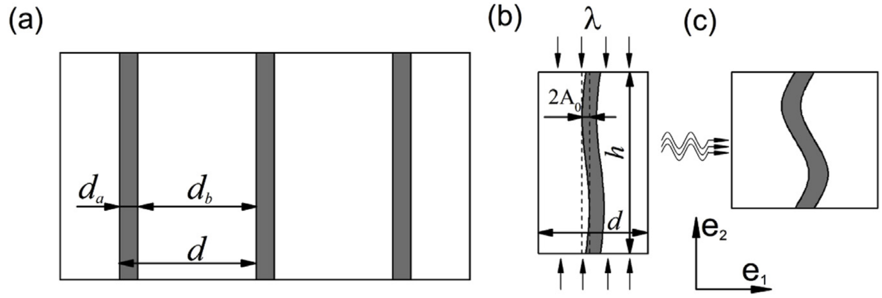

Fig. 1. (a) Periodic LCs, (b) Deformed unit cell, (c) Small amplitude wave propagation in the deformed unit cell.

3. Numerical simulation

We consider periodic layered composites consisted of two alternating hyperelastic phases with initial volume fractions $v_a = d_a/d$ and $v_b = 1 - v_a$ (see Fig. 1(a)). Here and thereafter, the quantities corresponding to phase a and phase b are denoted by subscripts $(\bullet)_a$ and $(\bullet)_b$, respectively. The constitutive behavior of each phase is defined through the extended neo-Hookean strain energy density function

$$W(\mathbf{F}_\xi) = \frac{\mu_\xi}{2}(\mathbf{F}_\xi : \mathbf{F}_\xi - 3) - \mu_\xi \ln(J_\xi) + \left(\frac{K_\xi}{2} - \frac{\mu_\xi}{3}\right)(J_\xi - 1)^2, \tag{9}$$

where μ_ξ is the initial shear modulus, K_ξ is the bulk modulus, subscript ξ stands for a or b. The compressibility of the material is defined by the ratio K_ξ/μ_ξ.

In order to detect the onset of instability of LCs, and obtain the corresponding critical stretch ratio λ^{cr} and critical wavelength l^{cr} (or critical wavenumber k^{cr}), the Bloch-Floquet analysis is used (for details, see Slesarenko and Rudykh, 2017; Triantafyllidis and Maker, 1985). The microscopic instability is associated with the existence of bifurcation at a non-zero critical wavenumber k^{cr}, which defines the buckling mode of the structure through the critical wavelength $l^{cr} = 2\pi/k^{cr}$. The specific case of so-called long wave mode, $k^{cr} \to 0$, can be detected by the loss of ellipticity analysis for the effective elastic modulus tensor. The obtained information about the critical wavelengths is used in the subsequent postbuckling analysis (and elastic wave propagation in the postbuckling regime). A unit cell with height $h = l^{cr}$ is constructed in the finite element model, and small amplitude imperfections are introduced in the form of $X_1 = \mathrm{A}_0 \cos\left(\frac{2\pi X_2}{h}\right)$ imposed on the initial geometry of the stiffer layer (see Fig. 1(b)). In particular, through checking different weights (A_0/d_a) of the imperfections, we find that $\mathrm{A}_0/d_a = 10^{-3}$ is proper to trigger bifurcation and enough precise to capture the development of the instability induced wavy patterns. The periodic boundary conditions of displacement are imposed on the unit cell, and the mechanical loading is applied in terms of average deformation gradient, which is used in the displacement imposed periodic boundary conditions on the unit cell (see Fig. 1(b)). The obtained numerical solution for the finitely deformed state is used in the subsequent small amplitude wave propagation analysis. This has been done by employing the Bloch wave numerical analysis (implemented in the finite element code, for details, see Bertoldi and Boyce, 2008a; Galich et al., 2017b; Slesarenko and Rudykh, 2017; Li et al., 2018b). Thus, the dispersion curves for elastic waves propagating in finitely deformed compressible LCs are obtained.

4. Results

4.1. Instability

We start from consideration of the influence of compressibility on the onset of instability and the corresponding critical wavelengths. Fig. 2 shows the dependence of critical stretch ratio λ^{cr} (a, c) and critical wavenumber $\widetilde{k}^{cr}$ (b, d) on the compressibility of LCs with neo-Hookean phases. Both phases are characterized by identical compressibility ($K_a/\mu_a = K_b/\mu_b = K/\mu$). The critical wavenumber is normalized as $\widetilde{k}^{cr} = k^{cr}d/(2\pi)$. For completeness, we show also the linear elastic material estimates denoted by the short-dashed black (Rosen, 1965) and by dotted blue curves (Parnes and Chiskis, 2002).[1] The circular points denote the numerical results for LCs with neo-Hookean phases. Hollow and solid symbols correspond to microscopic and macroscopic instabilities, respectively. Note that we also add the curves connecting the symbols, and these curves do not represent the actual data, but indicate the trends in the dependencies only.

Compressible LCs are observed to be more stable; in particular, the critical stretch ratio increases with a decrease in compressibility (an increase in K/μ), see Fig. 2 (a, c). This stabilizing effect may be due to the additional freedom in accommodating deformation in compressible LCs as compared to the constrained incompressible LCs. The linear estimates and nonlinear analysis predict similar trends of the dependence of critical stretch on compressibility. However, the nonlinear analysis predicts earlier onsets of instabilities. Moreover, for composites with lower stiffness ratio, significant differences in linear and nonlinear predictions of critical wavenumber are observed (see Fig. 2(d)). The LCs with lower shear modulus contrasts require larger deformation for onset of instability; therefore, the nonlinear behavior (not accounted in the linear estimates) becomes more prominent.

Remarkably, compressible LCs are found to develop instabilities on microscopic length-scales, while LCs with higher incompressibility (larger K/μ) buckle in the long wave mode. For example, in LC with $\mu_a/\mu_b = 100$, we observe a switch in buckling modes from microscopic instability to macroscopic instability indicated by the void (microscopic) and filled (macroscopic) red circles in Fig. 2(a and b). Similar transitions from microscopic to macroscopic instability modes in incompressible fiber composites happen when the shear moduli contrast is increased beyond a certain threshold value (Slesaranko and Rudykh, 2017). For compressible LCs, the observed macro-to-micro mode switch (at certain threshold compressibility value) may be attributed to the compressibility-induced reduction in the effective stiffness ratio between the phases; thus, leading to the development of microscopic instabilities. Finally, we note that the critical stretch ratio of neo-Hookean LCs attains the analytical estimation for incompressible neo-Hookean LCs (Triantafyllidis and Maker, 1985) as the incompressibility parameter is increased.

Next, we examine the influence of compressibility on instabilities in LCs with different volume fractions. Fig. 3 shows the critical stretch ratio λ^{cr} (a) and normalized critical wavenumber $\widetilde{k}^{cr}$ (b) as functions of compressibility for LCs with $\mu_a/\mu_b = 100$. The square, triangle, and circle symbols correspond to the LCs with $v_a = 0.04,\ 0.07,$ and 0.09, respectively. The black points correspond to the results of LCs with identical phase compressibility, while the red points correspond to LCs with nearly incompressible matrix ($K_b/\mu_b = 10^3$), and stiffer layers with

[1] The compressibility of linear elastic material is related to that of neo-Hookean material by Poisson's ratio $\nu = \frac{3K/\mu - 2}{6K/\mu + 2}$.

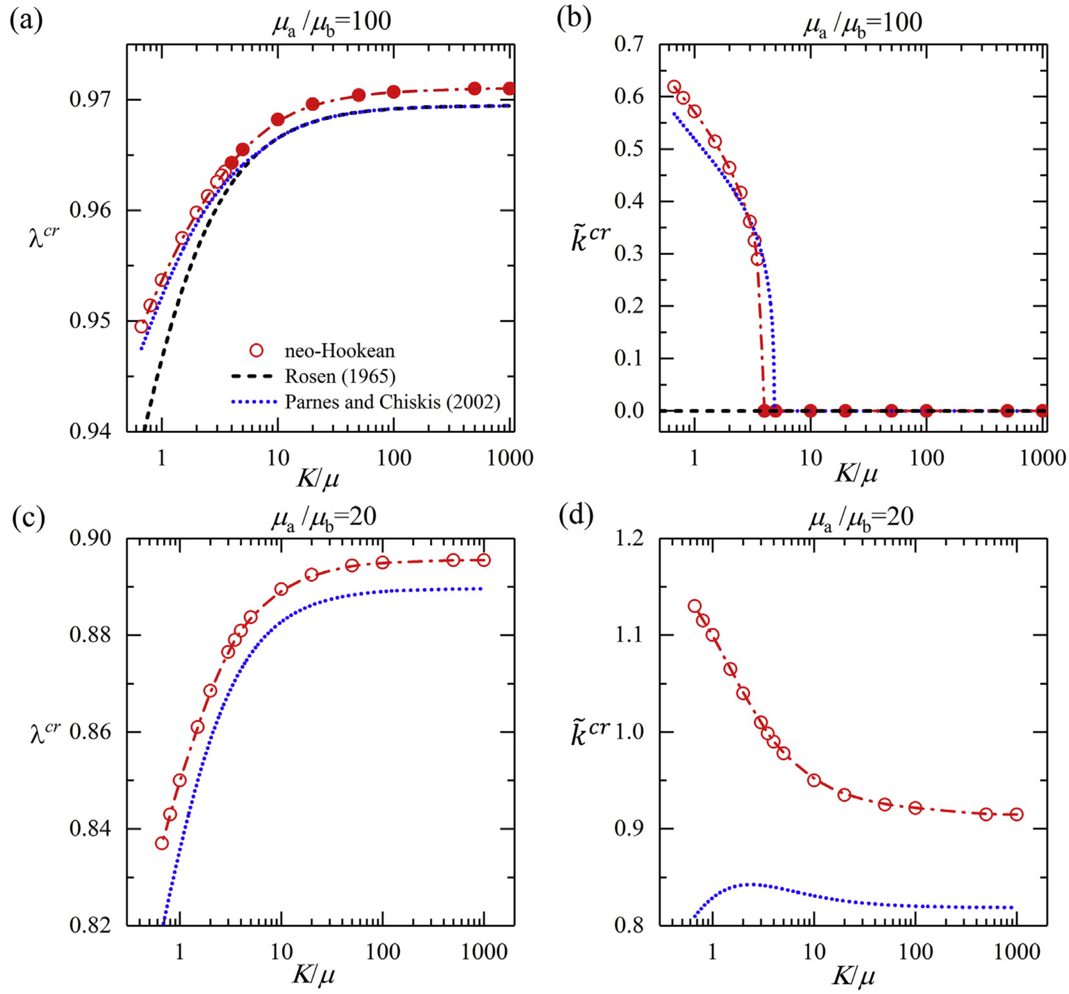

Fig. 2. Dependence of critical stretch ratio λ^{cr} (a, c) and critical wavenumber $\tilde{k}^{cr}$ (b, d) on the compressibility of LCs with $v_a = 0.09$, $K_a/\mu_a = K_b/\mu_b$. Hollow symbols correspond to microscopic instabilities, while solid symbols correspond to macroscopic instabilities.

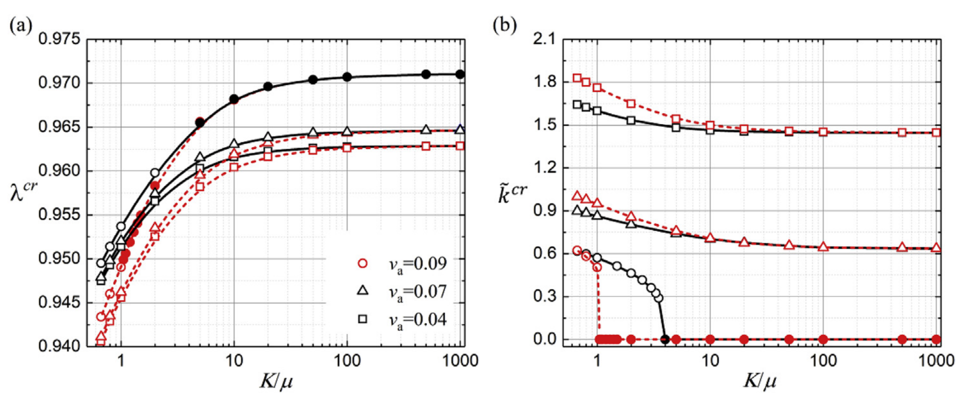

Fig. 3. Dependence of critical stretch ratio λ^{cr} (a) and critical wavenumber $\tilde{k}^{cr}$ (b) on the compressibility of LCs with $\mu_a/\mu_b = 100$. The black points correspond to LCs with identical compressibility; the red points correspond to LCs with nearly incompressible ($K_b/\mu_b = 10^3$) soft matrix. (For interpretation of the references to colour in this figure legend, the reader is referred to the Web version of this article.)

varying compressibility. Note that we consider the range of $K/\mu \geq 2/3$, such that the initial Poisson's ratio is positive (Shang and Lakes, 2007). Fig. 3(a) shows that the critical stretch ratio increases with a decrease in compressibility (an increase in K/μ). Note that LCs with $K/\mu \gtrsim 50$, critical stretch changes only slightly with an increase in K/μ. However, for LCs with $K/\mu \lesssim 10$, a decrease in compressibility (an increase in K/μ) results in a pronounced increase in critical stretch. For example, when compressibility of LC (with identical phase compressibility) is changed from $K/\mu = 50$ to 10^3, critical stretch of LC with $v_a = 0.04$ increases from $\lambda^{cr} = 0.9627$ to only 0.9628; whereas, a decrease in compressibility from $K/\mu = 2/3$ to 10 leads to an increase in critical stretch from $\lambda^{cr} = 0.9475$ to 0.9616. Fig. 3(b) shows the dependence of critical wavenumber $\tilde{k}^{cr}$ on the ratio of K/μ. We observe that the critical wavenumber decreases with a decrease in compressibility (i.e. increase in K/μ), the effect is more pronounced at the range of $K/\mu \lesssim 10$. We note that the LC with $v_a = 0.09$ exhibits a transition from finite wavelength mode to long wave instability mode at $K/\mu \approx 3.5$ for LCs with identical phase compressibility, $K/\mu \approx 1.1$ for LCs with nearly incompressible matrix and varying stiff layer compressibility, corresponding to a switch from microscopic instability to macroscopic instability.

For LCs with nearly incompressible matrix ($K_b/\mu_b = 10^3$), the influence of the stiffer layer compressibility on critical stretch ratio and wavenumber is more pronounced as compared to LC with identical phase compressibility (compare the red symbols with the black symbols in Fig. 3(a and b)). For example, for LC with $\nu_a = 0.07$, the change in compressibility of the stiffer layer from $K_a/\mu_a = 10^3$ to 2/3, leads to the changes in critical stretch ratio from $\lambda^{cr} = 0.965$ to 0.941, and critical wavenumber from $\widetilde{k}^{cr} = 0.64$ to 1.00. For LCs with identical phase compressibility, the same change in compressibility decreases the critical stretch ratio from $\lambda^{cr} = 0.965$ to 0.948, and increases the critical wavenumber from $\widetilde{k}^{cr} = 0.64$ to 0.90. One of the factors for the observed differences can be attributed to the change in the volume fraction of the stiffer layer under compression. For LCs with identical compressibility ($K_a/\mu_a = K_b/\mu_b$), the volume fraction of the stiffer layer is constant under contraction deformation (before the onset of instability). However, for LCs with nearly incompressible soft matrix and compressible stiff layers, the stiffer layer volume decreases under contraction deformation and the volume of the matrix remains constant. Thus, the volume fraction of the stiffer layer (in the deformed state) decreases. As a result, LCs with more compressible stiffer layers (with lower K_a/μ_a) buckle at larger strain levels, and develop wavy patterns of smaller wavelengths as compared to LCs with identical phase compressibility. However, the dependence of the wavelength on the stiffer layer compressibility changes for LCs with larger volume fractions, for which LCs may exhibit long wave instabilities (depending on the compressibility).

For LCs with identical phase compressibility, an increase in stiff layer volume fraction results in significant decrease in critical strain ($\varepsilon^{cr} = 1 - \lambda^{cr}$) and critical wavenumber. For example, for LC with nearly incompressible phases ($K_a/\mu_a = K_b/\mu_b = 10^3$), an increase in stiff layer volume fraction from $\nu_a = 0.04$ to 0.09 leads to an earlier onset of instabilities at $\varepsilon^{cr} = 0.029$ ($\varepsilon^{cr} = 0.037$ for $\nu_a = 0.04$), and leads to a switch in the instability mode from finite size $\widetilde{k}^{cr} = 1.45$ (for $\nu_a = 0.04$) to long wave mode ($\widetilde{k}^{cr} \to 0$ for $\nu_a = 0.09$).

Next we investigate the influence of compressibility on instabilities in LCs with different shear modulus contrasts. Fig. 4 shows the dependence of critical stretch ratio (a, c, e) and critical wavenumber (b, d, f) on compressibility. The circular, square, and triangle symbols correspond to the results of LCs with shear modulus contrasts $\mu_a/\mu_b = 20,\ 100$, and 500, respectively. The black and red points correspond to LCs with identical phase compressibility, and to LCs with nearly incompressible matrix ($K_b/\mu_b = 10^3$) and stiffer layer with varying compressibility, respectively. In agreement with the previous results, here we observe that the critical stretch ratio increases with a decrease in compressibility (i.e. increase in K/μ), and the critical wavenumber decreases with a decrease in compressibility (i.e. increase in K/μ). We observe that the critical strain for LC with lower shear modulus contrast is more sensitive to a change in compressibility. The compressibility has a more significant effect on the critical wavenumber of LC with higher shear modulus contrast. For instance, for LC with $\mu_a/\mu_b = 20$, the change of compressibility from $K_a/\mu_a = K_b/\mu_b = 10^3$ to 2/3, leads to the changes in critical strain from $\varepsilon^{cr} = 0.105$ to 0.163, and critical wavenumber from $\widetilde{k}^{cr} = 2.18$ to 2.57; thus the critical strain and wavenumber increase 55.24% and 17.89%, respectively. For LC with $\mu_a/\mu_b = 500$, the corresponding change in compressibility (from $K_a/\mu_a = K_b/\mu_b = 10^3$ to 2/3) leads to an increase in critical strain and wavenumber by 36.80% and 31.62%, respectively.

In addition, we also observe that an increase in the stiffer layer compressibility leads to a more significant increase in critical strain and wavenumber as compared to LC with identical phase compressibility in a wide range of shear modulus contrasts. This effect increases with an increase in shear modulus contrast (compare red and black symbols in Fig. 4). For instance, for the case of $\mu_a/\mu_b = 500$, the critical strain and wavenumber for LC with identical phase compressibility $K/\mu = 2/3$ are $\varepsilon^{cr} = 0.017$ and $\widetilde{k}^{cr} = 0.96$; and the critical strain and wavenumber for LC with $K_a/\mu_a = 2/3,\ K_b/\mu_b = 10^3$ are $\varepsilon^{cr} = 0.020$ and $\widetilde{k}^{cr} = 1.08$, increased by 17.65% and 12.5%, respectively (compared to LC with $K/\mu = 2/3$). Whereas for the case of $\mu_a/\mu_b = 20$, the critical strain and wavenumber for LC with $K_b/\mu_b = 10^3,\ K_a/\mu_a = 2/3$ increase by approximately 8% and 5%, respectively, when compared to the corresponding LC with identical phase compressibility $K/\mu = 2/3$.

LCs with stiffer layers (higher shear modulus contrasts) are more prone to instabilities, and develop buckling modes at smaller wavenumbers (larger wavelength). For example, for LC with nearly incompressible phases, namely, $K_a/\mu_a = K_b/\mu_b = 10^3$, the composite with $\mu_a/\mu_b = 20$ and 100 buckles at $\varepsilon^{cr} = 0.106$ to 0.037, and develops wavy pattern at $\widetilde{k}^{cr} = 2.18$ to 1.45, respectively.

To summarize, LCs with stronger role of stiffer layers are more prone to instabilities and develop buckling modes with larger wavelengths. Compressible LCs are found to be more stable thanks to the additional freedom in accommodating deformation as compared to the constrained incompressible LCs. There are compressibility-controlled switches in the LC buckling modes from macroscopic to microscopic instabilities. These switches may be a result of reduction in effective stiffness ratio between the phases arising from the deformation of compressible LC. Moreover, LCs with nearly incompressible matrix are more stable than the LCs with identical phase compressibility. This stabilizing effect can be attributed to a decrease in the compressible stiffer layer volume fraction (while the volume of nearly incompressible matrix remains almost constant).

4.2. Elastic waves in finitely deformed compressible laminates

Next, we consider elastic waves propagating in finitely deformed LCs in the direction perpendicular to the layers. For this case, Galich et al. (2017a) extended the results of Rytov (1956) to account for the effect of finite deformation on elastic wave propagation. The explicit results for neo-Hookean LCs by Galich et al. (2017a) clearly show that band gaps (BG) – frequency ranges where waves cannot propagate – of shear waves do not depend on deformation. This is because the deformation induced changes in geometries and local material properties compensate each other. However, once the deformation exceeds the critical stretch ratio, the stiffer layers develop wavy patterns and deformation becomes inhomogeneous in the phases. Therefore, the analytical solution – that assumes that the layers remain flat and deformation is homogeneous in each layer – reaches the limits of applicability. To overcome this limit and analyze the influence of compressibility on elastic wave propagation in finitely deformed compressible LCs, we make use of the finite element Bloch wave analysis superimposed on large deformations (Bertoldi and Boyce, 2008a, 2008b).

We start with illustrating the dispersion curves of the undeformed and deformed ($\lambda = 0.9$) LCs. The dispersion curves shown in Fig. 5 are for LC with $\nu_a = 0.04,\ \ \mu_a/\mu_b = 100,\ \rho_a/\rho_b = 1,\ K_a/\mu_a = K_b/\mu_b = 1$. The continuous curves correspond to shear waves, while the dashed curves are for pressure waves. The shaded grey and blue areas correspond to the shear wave band gaps (SBGs) and pressure wave band gaps (PBGs), respectively. Frequency is normalized as $f_n = \frac{\omega d}{2\pi}\sqrt{\overline{\rho_0}/\widetilde{\mu}}$, where ω is the angular frequency, $\overline{\rho_0} = \rho_{0a}\nu_a + \rho_{0b}\nu_b,\ \widetilde{\mu} = \left(\frac{\nu_a}{\mu_a} + \frac{\nu_b}{\mu_b}\right)^{-1}$. We note that the numerical results are in perfect agreement with the theoretical results (Galich et al., 2017a; Rytov, 1956) for the range of deformations, where the LCs remain stable. In the buckled deformed state at $\lambda = 0.9$ ($\lambda^{cr} = 0.9514$), the first SBG widens from $\Delta f_n = 0.020$ (in the undeformed state) to 0.024, and its upper boundary shifts from $f_n = 0.510$ to 0.524, the first PBG widens from $\Delta f_n = 0.031$ (in the undeformed state) to 0.032 and its upper boundary shifts from $f_n = 0.779$ to 0.767.

Next, we investigate the influence of deformation on the BG

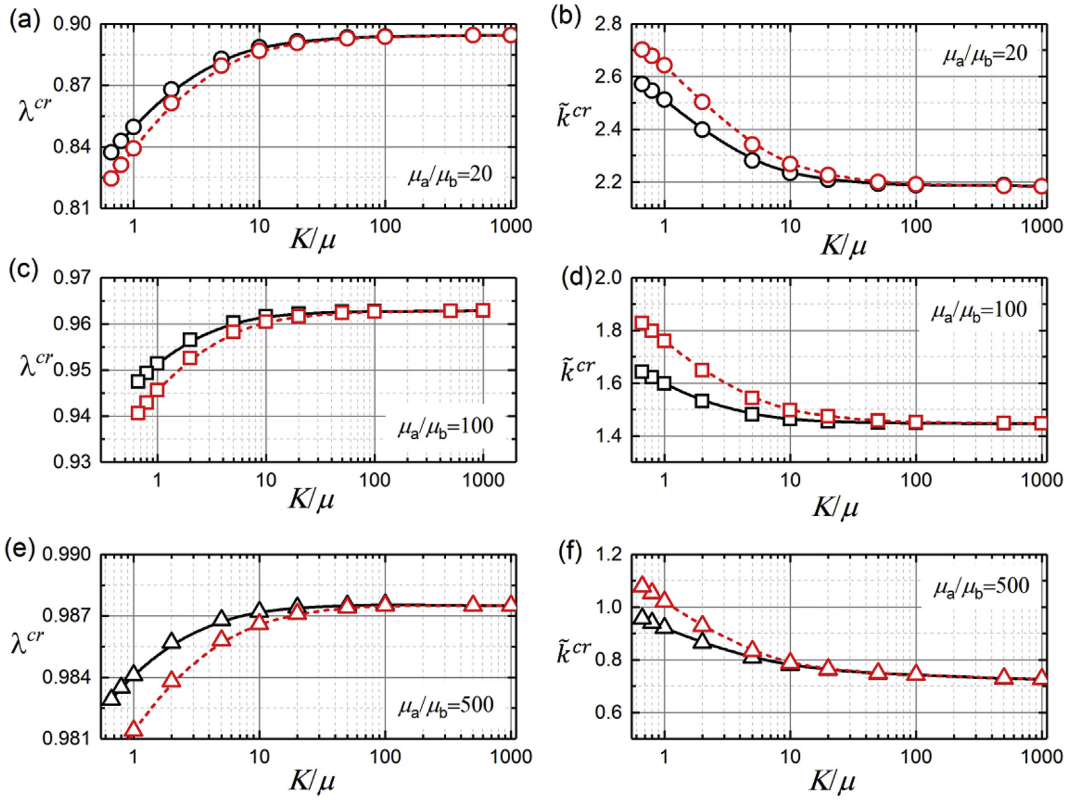

Fig. 4. Dependence of critical stretch ratio λ^{cr} ((a), (c), and (e)) and critical wavenumber $\widetilde{k}^{cr}$ ((b), (d), and (f)) on the compressibility of LCs with $v_a = 0.04$.

structure of nearly incompressible LCs. Fig. 6 shows evolutions of the first SBG (a) and wrinkle amplitude (b) as functions of deformation. The wrinkle amplitude is normalized as $\widetilde{A} = \frac{A}{d_a}$. The LC with $v_a = 0.04$, $\mu_a/\mu_b = 100$, $\rho_a/\rho_b = 1$ consists of nearly incompressible phases ($K_a/\mu_a = K_b/\mu_b = 10^3$), and it experiences microscopic instability at $\lambda^{cr} = 0.963$ with the critical wavenumber $\widetilde{k}^{cr} = 1.45$. To highlight the effect of instability induced wavy patterns on SBG, we show the results for the buckled LC and the flat LC (in which the wavy patterns are suppressed) under the same deformation. The analytical results (Galich et al., 2017a) for the first SBG of LC with flat layers is located at lower frequency boundary $f_n = 0.490$ and width $\Delta f_n = 0.020$, which is independent of deformation. Before the onset of instability ($\lambda^{cr} = 0.963$), the wavy pattern amplitude is negligible (see Fig. 6(b)), and LCs produce identical SBGs (see Fig. 6(a)). After the onset of instability, the LC develops wavy patterns, and the amplitude of wrinkles rapidly increases with an increase in deformation (see Fig. 6(b)). The appearance of the wavy patterns shifts up the location of SBG and expands its width. The effect is more significant for the upper frequency boundary of the BG. For example, the deformation of $\lambda = 0.9$ widens the SBG from $\Delta f_n = 0.020$ to 0.029 and shifts its upper frequency boundary from $f_n = 0.510$ to 0.520. We note that for the considered nearly incompressible LC ($K/\mu = 10^3$), PBGs are located at relatively high frequency ranges (compared to the first SBG). For example, according to the calculation that based on the results of Galich et al. (2017a), the lower boundary of the first SBG for considered LC in the undeformed state is $f_n = 0.490$ (with $\Delta f_n = 0.020$), while the lower boundary of the

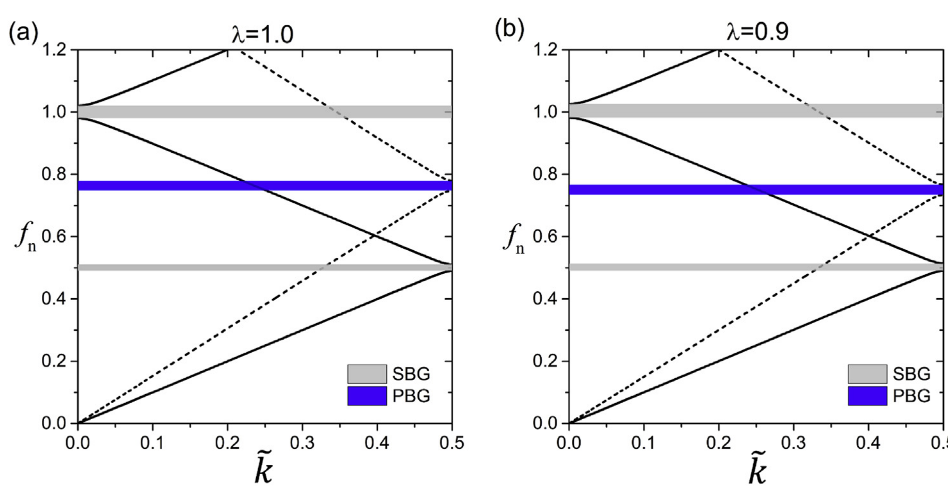

Fig. 5. Dispersion relations for shear (black continuous curves) and pressure (black dashed curves) waves in LC with $v_a = 0.04$, $\mu_a/\mu_b = 100$, $\rho_a/\rho_b = 1$, $K_a/\mu_a = K_b/\mu_b = 1$ in undeformed (a) and deformed (b) states. The shaded areas correspond to the shear (grey) and pressure (blue) wave BGs. (For interpretation of the references to colour in this figure legend, the reader is referred to the Web version of this article.)

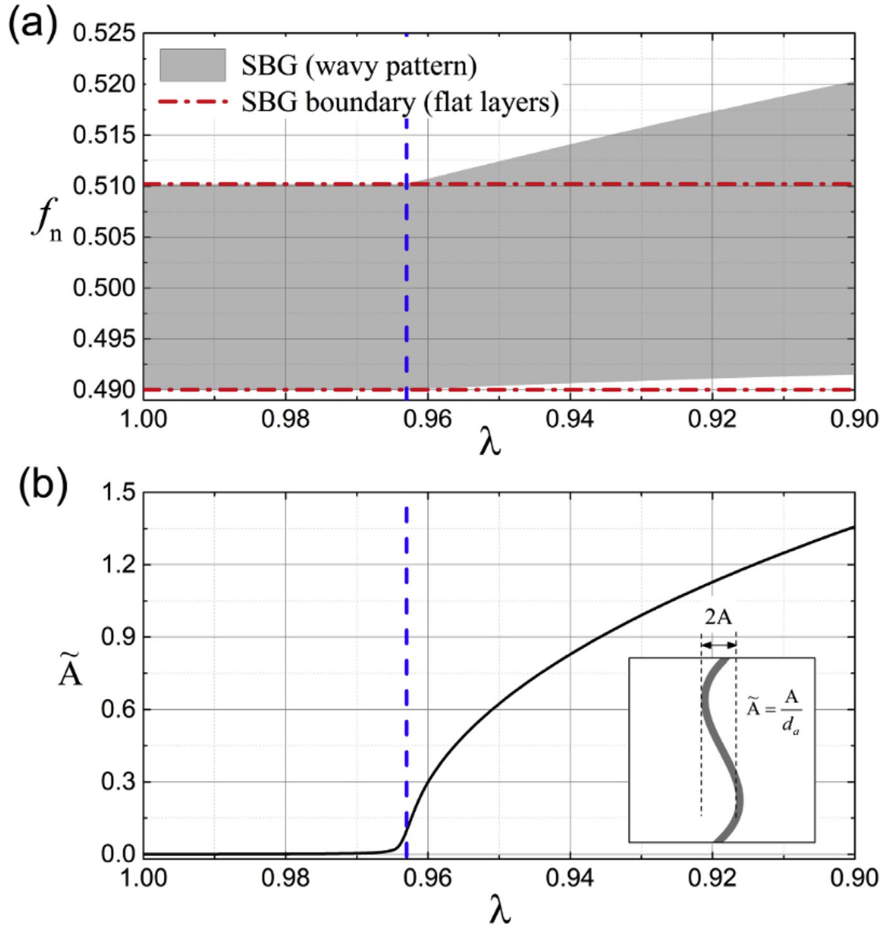

Fig. 6. Dependence of SBG (a) and wrinkle amplitude (b) on applied deformation for LC with $\nu_a = 0.04$, $\mu_a/\mu_b = 100$, $\rho_a/\rho_b = 1$, $K_a/\mu_a = K_b/\mu_b = 10^3$.

corresponding first PBG is $f_n = 15.51$ (with $\Delta f_n = 0.63$). The numerical investigation of PBGs in LCs with nearly incompressible phases requires a large number of calculated eigenfrequencies and is not considered here.

To illustrate the influence of deformation in compressible LCs, we show SBG (a), PBG (b), and wrinkle amplitude (c) as functions of deformation in Fig. 7. The results are given for the LC with $\nu_a = 0.04$, $\mu_a/\mu_b = 100$, $\rho_a/\rho_b = 1$, $K_a/\mu_a = K_b/\mu_b = 1$. The considered LC experiences microscopic instability at $\lambda^{cr} = 0.951$ with the critical wave number $\widetilde{k}^{cr} = 1.60$. For the SBG (shown in Fig. 7(a)), we observe that the appearance of the wavy patterns leads to widening of the SBG. Moreover, the SBG is shifted towards higher frequency range after the applied deformation attains the critical stretch level; a further increase in strain level (decrease in stretch ratio) leads to an increase in the width of the SBG. In particular, the applied deformation of $\lambda = 0.9$ widens the SBG from $\Delta f_n = 0.020$ to 0.023 and shifts its upper frequency boundary from $f_n = 0.510$ to 0.514. Thus, for highly compressible LCs, the influence of instability induced wavy patterns on the widths of SBGs is weaker than the one in nearly incompressible LCs (shown in Fig. 6(a)). This happens because an increase in compressibility (decrease in K/μ) leads to a decrease in wavy pattern amplitude. For example, the amplitudes in LCs with nearly incompressible ($K_a/\mu_a = K_b/\mu_b = 10^3$) and highly compressible phases ($K_a/\mu_a = K_b/\mu_b = 1$) at the deformation of $\lambda = 0.9$ are $\widetilde{A} = 1.36$ and 1.10, respectively.

For PBG (shown in Fig. 7(b)), the LCs with wavy patterns and flat layers produce almost identical PBGs for the range of deformation prior to the onset of instability ($\lambda^{cr} = 0.951$). After the onset of instability, however, the instability induced wavy patterns widen the PBG and shift it towards higher frequency range. This effect is more significant on the upper frequency boundary of PBG. For example, compared to the LC with flat layers, the PBG of LC with wavy patterns widens from $\Delta f_n = 0.030$ to 0.032 and its upper frequency boundary shifts from $f_n = 0.764$ to 0.767 at the deformation of $\lambda = 0.9$. This is similar to the previous results for SBGs (see Fig. 6(a), Fig. 7(a)).

Fig. 8 shows the dependence of SBG (a), PBG (b), and wrinkle amplitude (c) on the compressibility parameter K/μ. The results are given for LCs with $\nu_a = 0.04$, $\mu_a/\mu_b = 100$, $\rho_a/\rho_b = 1$ subjected to a contraction deformation of $\lambda = 0.9$. For LCs with flat layers, we observe that compressibility does not affect the SBGs (see Fig. 8 (a)) – in full agreement with the analytical results[2] of Galich et al. (2017a). For LCs with wavy patterns, however, we observe that the SBGs are widened and the SBG locations are shifted towards higher frequency ranges. This effect increases with a decrease in compressibility (i.e. increase in K/μ). For example, when the compressibility changes from $K/\mu = 0.67$ to 10^3, the width of SBG of LC with identical compressibility increases from $\Delta f_n = 0.023$ to 0.029. This is due to the fact that an increase in K/μ leads to an increase in wrinkle amplitude (see Fig. 8(c)). Moreover, we note that LCs with identical phase compressibility show larger wrinkle amplitudes as compared to LCs with nearly incompressible matrix (see Fig. 8(c)). However, LCs with nearly incompressible matrix show more significant widening of SBGs (Fig. 8(a)). This indicates that the tunability of the SBG is governed by a complicated interplay of the local material property and geometry changes; these effects are discussed below along with the illustrations in Fig. 10.

[2] The change in geometry induced by deformation is fully compensated by the corresponding change in material properties in neo-Hookean laminates with compressible and incompressible phases.

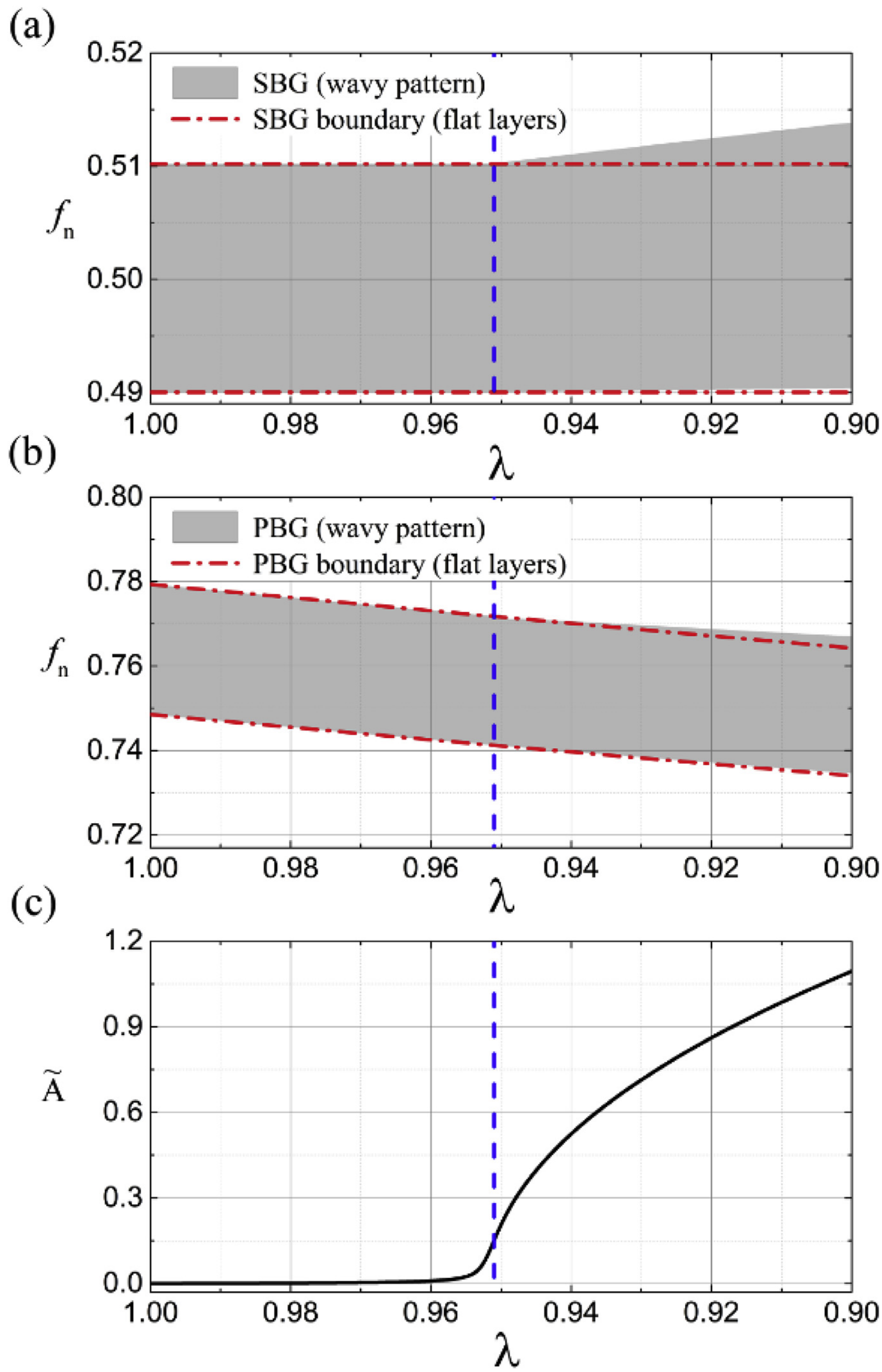

Fig. 7. Dependence of SBG (a), PBG (b), and wrinkle amplitude (c) on applied deformation for LC with $v_a = 0.04$, $\mu_a/\mu_b = 100$, $\rho_a/\rho_b = 1$, $K_a/\mu_a = K_b/\mu_b = 1$.

For PBGs in highly compressible LCs, we observe that the instability induced wavy patterns expand the widths and shift their locations to higher frequency ranges (as compared to the LCs with flat layers). For example, for LC with $K/\mu = 0.67$, the appearance of wavy patterns expands the width of PBG from $\Delta f_n = 0.028$ to 0.031 and shifts its upper frequency boundary from $f_n = 0.721$ to 0.724. Whereas with the decrease of compressibility (i.e. increase in K/μ), the effect of wavy patterns on PBG gradually changes from expanding the BG width and shifting its location to higher frequency range, to narrowing the BG width and shifting its location to lower frequency range (see Fig. 8 (b)). For example, for LC with $K/\mu = 10$, the wavy patterns narrow the width of PBG from $\Delta f_n = 0.062$ to 0.058, and shift its upper frequency boundary from $f_n = 1.565$ to 1.559. For the considered cases, the transition point at which the effect of wavy patterns on PBGs changes from expanding to narrowing the BG widths is at $K/\mu \approx 4$. We note that for the considered LCs with nearly incompressible soft matrix ($K_b/\mu_b = 10^3$), PBGs are located at relatively high frequency ranges (compared to the first SBG). Thus, numerical investigation of PBGs in LCs with nearly incompressible soft matrix requires a large number of calculated eigenfrequencies and is not considered here.

Next, we examine the so-called complete BGs where neither shear nor pressure waves can propagate. Fig. 9 show the dependence of SBG and PBG on the compressibility for LCs with $v_a = 0.04$, $\mu_a/\mu_b = 100$, $\rho_a/\rho_b = 1$ in the undeformed and deformed buckled ($\lambda = 0.9$ shown in Fig. 9(b)) states. The shaded gray, blue, and black areas correspond to the shear wave, pressure wave, and complete BGs, respectively. In the undeformed state, the compressibility has no influence on SBGs. In the buckled deformed state, however, the

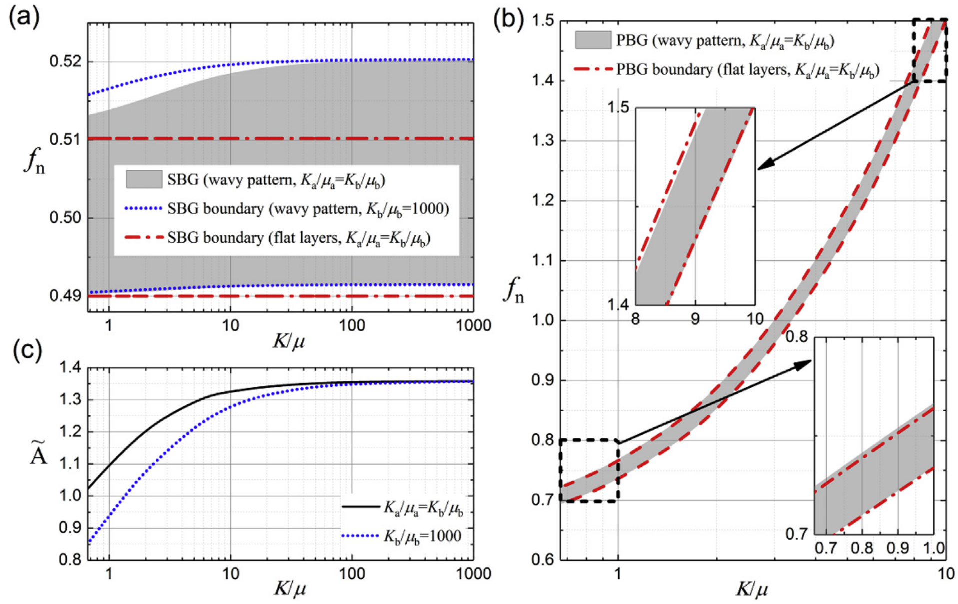

Fig. 8. Dependence of SBG (a), PBG (b), and wrinkle amplitude (c) on the compressibility of LCs with $v_a = 0.04$, $\mu_a/\mu_b = 100$, $\rho_a/\rho_b = 1$ under deformation of $\lambda = 0.9$.

locations of SBGs shift slightly, but the locations of PBGs are significantly shifted towards lower frequency ranges; this is similar to the observations in Figs. 7 and 8. Consequently, deformation can induce complete BG in a specific frequency range while the undeformed LCs do not produce complete BG in that frequency range. For example, for LC with $K/\mu = 3.5$, we observe the complete BG in the frequency range from $f_n = 1.002$ to 1.028, but there is no complete BG in this frequency range for the same LC in the undeformed state.

Finally, we examine the influence of deformation induced geometrical changes on band gaps. To this end, we analyze the evolution of BGs in stress-free configurations with the corresponding geometrical changes; and we compare these to the results for the deformed configurations (accounting for both geometrical and local material property changes). Fig. 10 shows the SBGs (a) and PBGs (b) of the deformed LC and stress-free LC (with the corresponding geometrical change only) as functions of stretch ratio. The results are given for LC with $v_f = 0.04$, $\mu_a/\mu_b = 100$, $\rho_a/\rho_b = 1$, $K_a/\mu_a = K_b/\mu_b = 5$. The LC experiences the microscopic instability at $\lambda^{cr} = 0.960$ with the critical wavenumber $\widetilde{k}^{cr} = 1.48$. Prior to the onset of instability ($\lambda^{cr} = 0.960$), the geometrical changes shift the SBG towards lower frequencies (see Fig. 10(a)). This effect however, is fully compensated by the corresponding deformation induced changes in local material properties (Galich et al., 2017a). Thus, the SBG of the deformed LC are independent of the applied deformation in the stable regime. However, upon the onset of instability, the SBG widens as the applied deformation is further increased. At this post-buckling regime, the corresponding SBG of the stress-free LC also widens with deformation. However, the width of the actual SBG (in the deformed LC) is smaller than that of the stress-free LC. Moreover, the actual SBG is shifted towards higher frequencies, whereas the geometrical changes push the SBG down towards lower frequencies. Thus, the instability induced changes in local material properties start prevailing over the geometrical changes in their influence on the SBG.

Next, we consider PBGs in the deformed and stress-free LCs. The PBGs are shifted towards lower frequencies. The location of the PBG of the deformed LC is lower than that of the stress-free LC (see Fig. 10(b)). Therefore, we can conclude that both geometrical and local material changes shift down the location of PBG. Compared to the PBG in the undeformed state (the corresponding PBG width is $\Delta f_n = 0.051$), the PBGs of the stress-free and deformed LCs are $\Delta f_n = 0.053$ and 0.045 (at $\lambda = 0.9$), respectively. Thus, the deformation induced changes in local material property narrow the width of PBG. We note that the

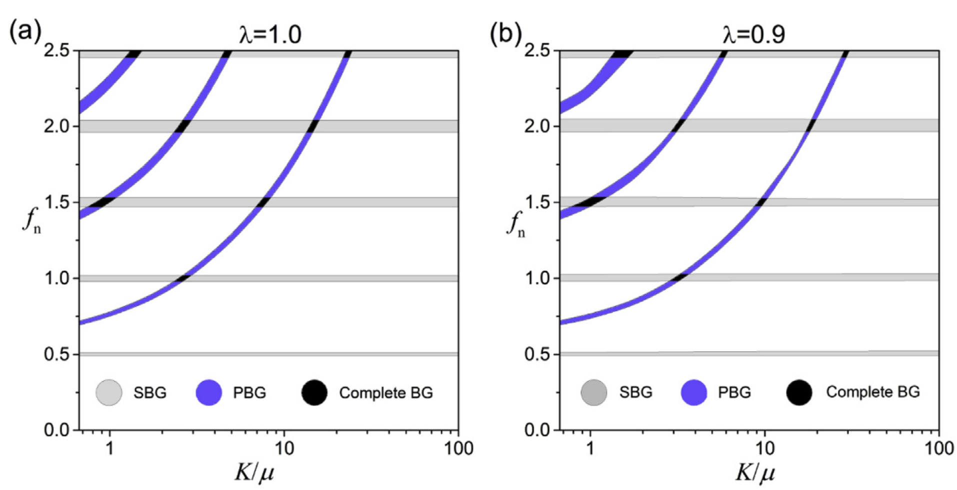

Fig. 9. Dependence of BG on the compressibility of LCs with $v_a = 0.04$, $\mu_a/\mu_b = 100$, $\rho_a/\rho_b = 1$ in the undeformed (a) and deformed (b) states.

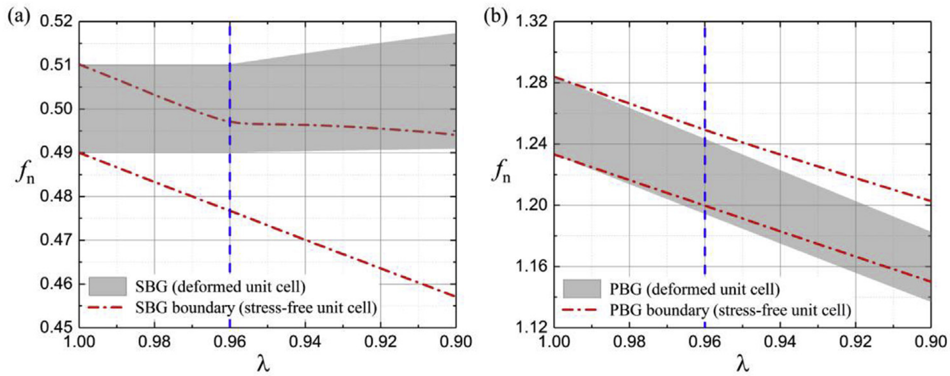

Fig. 10. Dependence of SBGs (a) and PBGs (b) on deformation in LCs with $v_f = 0.04$, $\mu_a/\mu_b = 100$, $\rho_a/\rho_b = 1$, $K_a/\mu_a = K_b/\mu_b = 5$.

geometrical changes play a more significant role in affecting the location of PBG. For example, applied deformation of $\lambda = 0.9$ shifts the lower frequency boundary of the PBG of stress-free unit cell from $f_n = 1.233$ (undeformed state) to 1.150, whereas the same deformation shifts the lower frequency boundary of the PBG of the deformed unit cell from $f_n = 1.233$ (undeformed state) only to 1.137.

In summary, the instability induced wavy patterns results in tunability of the widths and locations of SBGs (that are not tunable by deformation in LCs with neo-Hookean phases in the stable regime); this tunability, however, is not significant in comparison to the tunability of the PBGs (mainly through deformation induced changes in layer thickness), leading to the tunability of complete BGs (where neither shear nor pressure wave can propagate) by deformation.

5. Conclusions

We have examined the elastic instability and wave propagation in finitely deformed LCs with compressible neo-Hookean phases. The LCs with stronger role of stiffer layers (higher stiffness ratio and/or stiffer layer volume fraction) buckle earlier and develop buckling modes at smaller wavenumbers (larger wavelengths). Compressible LCs, however, are more stable and develop wavy patterns at smaller wavelengths. This stabilizing effect of compressibility may be attributed to the additional freedom to accommodate deformation as compared to the constrained incompressible LCs. We also observed the compressibility-controlled switches in the LC buckling modes from macroscopic to microscopic instabilities. These switches may be because applied deformation on compressible LC leads to a reduction in effective stiffness ratio between the phases. Moreover, LCs with identical phase compressibility are more prone to onset of instabilities as compared to the composites with nearly incompressible matrix, this happens because the contraction deformation results in a decrease in the stiffer layer volume fraction for LCs with nearly incompressible matrix.

Next, we have examined the elastic wave propagation in finitely deformed LCs in the direction perpendicular to the layers. We have found that the instability induced wavy patterns lead to widening of the SBG (mostly driven by the deformation induced geometrical changes), and shifts it towards higher frequency range (mostly driven by the deformation induced changes in local material property). Deformation significantly shifts the location of PBG to lower frequencies – mainly through the corresponding deformation induced changes in layer thickness – in addition to some tunability in the width of the PBG.

Acknowledgements

The authors acknowledge the support of Israel Science Foundation through grants №1550/15 and 1973/15, and US-Israel Binational Science Foundation through grant №2016284. JL thanks the support of Lady Davis graduate student fellowship. VS thanks the Technion postdoctoral fellowship.

References

Agoras, M., Lopez-Pamies, O., Ponte Castañeda, P., 2009. Onset of macroscopic instabilities in fiber-reinforced elastomers at finite strain. J. Mech. Phys. Solid. 57, 1828–1850.
Babaee, S., Viard, N., Wang, P., Fang, N.X., Bertoldi, K., 2016. Harnessing deformation to switch on and off the propagation of sound. Adv. Mater. 28, 1631–1635.
Bayat, A., Gordaninejad, F., 2015. Band-gap of a soft magnetorheological phononic crystal. J. Vib. Acoust. 137, 011013.
Bertoldi, K., Boyce, M.C., 2008a. Wave propagation and instabilities in monolithic and periodically structured elastomeric materials undergoing large deformations. Phys. Rev. B 78, 184107.
Bertoldi, K., Boyce, M.C., 2008b. Mechanically triggered transformations of phononic band gaps in periodic elastomeric structures. Phys. Rev. B 77, 052105.
Bigoni, D., Guenneau, S., Movchan, A.B., Brun, M., 2013. Elastic metamaterials with inertial locally resonant structures: application to lensing and localization. Phys. Rev. B 87, 174303.
Casadei, F., Delpero, T., Bergamini, A., Ermanni, P., Ruzzene, M., 2012. Piezoelectric resonator arrays for tunable acoustic waveguides and metamaterials. J. Appl. Phys. 112, 064902.
Celli, P., Gonella, S., 2015. Manipulating waves with LEGO ® bricks: a versatile experimental platform for metamaterial architectures. Appl. Phys. Lett. 107, 081901.
Celli, P., Gonella, S., Tajeddini, V., Muliana, A., Ahmed, S., Ounaies, Z., 2017. Wave control through soft microstructural curling: bandgap shifting, reconfigurable anisotropy and switchable chirality. Smart Mater. Struct. 26, 035001.
Chen, Q., Elbanna, A., 2016. Modulating elastic band gap structure in layered soft composites using sacrificial interfaces. J. Appl. Mech. 83, 111009.
Chen, Y., Wang, L., 2016. Bio-inspired heterogeneous composites for broadband vibration mitigation. Sci. Rep. 5, 17865.
dell'Isola, F., Giorgio, I., Pawlikowski, M., Rizzi, N.L., 2016. Large deformations of planar extensible beams and pantographic lattices: heuristic homogenization, experimental and numerical examples of equilibrium. Proc. R. Soc. A Math. Phys. Eng. Sci. 472, 20150790.
Destrade, M., Ogden, R.W., 2011. On magneto-acoustic waves in finitely deformed elastic solids. Math. Mech. Solid 16, 594–604.
Fomenko, S.I., Golub, M.V., Zhang, C., Bui, T.Q., Wang, Y.S., 2014. In-plane elastic wave propagation and band-gaps in layered functionally graded phononic crystals. Int. J. Solid Struct. 51, 2491–2503.
Galich, P.I., Fang, N.X., Boyce, M.C., Rudykh, S., 2017a. Elastic wave propagation in finitely deformed layered materials. J. Mech. Phys. Solid. 98, 390–410.
Galich, P.I., Rudykh, S., 2017. Shear wave propagation and band gaps in finitely deformed dielectric elastomer laminates: long wave estimates and exact solution. J. Appl. Mech. 84, 091002.
Galich, P.I., Rudykh, S., 2016. Manipulating pressure and shear waves in dielectric elastomers via external electric stimuli. Int. J. Solid Struct. 91, 18–25.
Galich, P.I., Slesarenko, V., Li, J., Rudykh, S., 2018. Elastic instabilities and shear waves in hyperelastic composites with various periodic fiber arrangements. Int. J. Eng. Sci. 130, 51–61.
Galich, P.I., Slesarenko, V., Rudykh, S., 2017b. Shear wave propagation in finitely deformed 3D fiber-reinforced composites. Int. J. Solid Struct. 110–111, 294–304.
Gao, C., Li, Y., 2017. Tuning the wrinkling patterns of an interfacial/coating layer via a regulation interphase. Int. J. Solid Struct. 104–105, 92–102.
Gei, M., Roccabianca, S., Bacca, M., 2011. Controlling bandgap in electroactive polymer-based structures. IEEE/ASME Trans. Mechatronics 16, 102–107.
Geymonat, G., Muller, S., Triantafyllidis, N., 1993. Homogenization of nonlinearly elastic materials, microscopic bifurcation and macroscopic loss of rank-one convexity. Arch. Ration. Mech. Anal. 122, 231–290.
Harne, R.L., Urbanek, D.C., 2017. Enhancing broadband vibration energy suppression using local buckling modes in constrained metamaterials. J. Vib. Acoust. 139, 061004.
Huang, Y., Zhang, C.L., Chen, W.Q., 2014. Tuning band structures of two-dimensional

phononic crystals with biasing fields. J. Appl. Mech. 81, 091008.
Jandron, M.A., Henann, D., 2017. Exploring phononic crystal tunability using dielectric elastomers. J. Acoust. Soc. Am. 141, 3743.
Javid, F., Wang, P., Shanian, A., Bertoldi, K., 2016. Architected materials with ultra-low porosity for vibration control. Adv. Mater. 28, 5943–5948.
Li, G.Y., Zheng, Y., Cao, Y.P., Feng, X.Q., Zhang, W.Y., 2016. Controlling elastic wave propagation in a soft bilayer system via wrinkling-induced stress patterns. Soft Matter 12, 4204–4213.
Li, J., Slesarenko, V., Galich, P.I., Rudykh, S., 2018a. Instabilities and pattern formations in 3D-printed deformable fiber composites. Compos. B Eng. 148, 114–122.
Li, J., Slesarenko, V., Galich, P.I., Rudykh, S., 2018b. Oblique shear wave propagation in finitely deformed layered composites. Mech. Res. Commun. 87, 21–28.
Li, Y., Kaynia, N., Rudykh, S., Boyce, M.C., 2013. Wrinkling of interfacial layers in stratified composites. Adv. Eng. Mater. 15, 921–926.
Matlack, K.H., Bauhofer, A., Krödel, S., Palermo, A., Daraio, C., 2016. Composite 3D-printed metastructures for low-frequency and broadband vibration absorption. Proc. Natl. Acad. Sci. Unit. States Am. 113, 8386–8390.
Meaud, J., Che, K., 2017. Tuning elastic wave propagation in multistable architected materials. Int. J. Solid Struct. 122–123, 69–80.
Merodio, J., Ogden, R.W., 2005. Mechanical response of fiber-reinforced incompressible non-linearly elastic solids. Int. J. Non Lin. Mech. 40, 213–227.
Merodio, J., Ogden, R.W., 2003. Instabilities and loss of ellipticity in fiber-reinforced compressible non-linearly elastic solids under plane deformation. Int. J. Solid Struct. 40, 4707–4727.
Merodio, J., Ogden, R.W., 2002. Material instabilities in fiber-reinforced nonlinearly elastic solids under plane deformation. Arch. Mech. 54, 525–552.
Miniaci, M., Krushynska, A., Movchan, A.B., Bosia, F., Pugno, N.M., 2016. Spider web-inspired acoustic metamaterials. Appl. Phys. Lett. 109, 071905.
Nestorović, M.D., Triantafyllidis, N., 2004. Onset of failure in finitely strained layered composites subjected to combined normal and shear loading. J. Mech. Phys. Solid. 52, 941–974.
Ogden, R.W., 1997. Non-linear Elastic Deformations. Dover Publications, New York.
Parnes, R., Chiskis, A., 2002. Buckling of nano-fibre reinforced composites: a re-examination of elastic buckling. J. Mech. Phys. Solid. 50, 855–879.
Rosen, B.W., 1965. Mechanics of composite strengthening. In: Fibre Composite Materials. American Society for Metals, Ohio, pp. 37–75.
Rudykh, S., Boyce, M.C., 2014. Transforming wave propagation in layered media via instability-induced interfacial wrinkling. Phys. Rev. Lett. 112, 034301.
Rudykh, S., Debotton, G., 2012. Instabilities of hyperelastic fiber composites: micromechanical versus numerical analyses. J. Elasticity 106, 123–147.
Rytov, S., 1956. Acoustical properties of a thinly laminated medium. Sov. Phys. Acoust. 2, 68–80.
Shan, S., Kang, S.H., Wang, P., Qu, C., Shian, S., Chen, E.R., Bertoldi, K., 2014. Harnessing multiple folding mechanisms in soft periodic structures for tunable control of elastic waves. Adv. Funct. Mater. 24, 4935–4942.
Shang, X., Lakes, R.S., 2007. Stability of elastic material with negative stiffness and negative Poisson's ratio. Phys. Status Solidi Basic Res. 244, 1008–1026.
Slesarenko, V., Galich, P.I., Fang, N.X., Li, J., Rudykh, S., 2018. Foreshadowing elastic instabilities by negative group velocity in soft composites. Appl. Phys. Lett. 113, 031901.
Slesarenko, V., Rudykh, S., 2017. Microscopic and macroscopic instabilities in hyperelastic fiber composites. J. Mech. Phys. Solid. 99, 471–482.
Slesarenko, V., Rudykh, S., 2016. Harnessing viscoelasticity and instabilities for tuning wavy patterns in soft layered composites. Soft Matter 12, 3677–3682.
Srivastava, A., 2016. Metamaterial properties of periodic laminates. J. Mech. Phys. Solid. 96, 252–263.
Trainiti, G., Rimoli, J.J., Ruzzene, M., 2016. Wave propagation in undulated structural lattices. Int. J. Solid Struct. 97–98, 431–444.
Triantafyllidis, N., Maker, B.N., 1985. On the comparison between microscopic and macroscopic instability mechanisms in a class of fiber-reinforced composites. J. Appl. Mech. 52, 794.
Wang, P., Casadei, F., Shan, S., Weaver, J.C., Bertoldi, K., 2014. Harnessing buckling to design tunable locally resonant acoustic metamaterials. Phys. Rev. Lett. 113, 014301.
Wang, P., Shim, J., Bertoldi, K., 2013. Effects of geometric and material nonlinearities on tunable band gaps and low-frequency directionality of phononic crystals. Phys. Rev. B 88, 014304.
Wood, B., Pendry, J.B., Tsai, D.P., 2006. Directed subwavelength imaging using a layered metal-dielectric system. Phys. Rev. B 74, 115116.
Wu, M.L., Wu, L.Y., Yang, W.P., Chen, L.W., 2009. Elastic wave band gaps of one-dimensional phononic crystals with functionally graded materials. Smart Mater. Struct. 18, 115013.
Xu, J., Jiang, X., Fang, N., Georget, E., Abdeddaim, R., Geffrin, J.M., Farhat, M., Sabouroux, P., Enoch, S., Guenneau, S., 2015. Molding acoustic, electromagnetic and water waves with a single cloak. Sci. Rep. 5, 10678.
Yang, W.P., Chen, L.W., 2008. The tunable acoustic band gaps of two-dimensional phononic crystals with a dielectric elastomer cylindrical actuator. Smart Mater. Struct. 17, 015011.
Zhang, P., Parnell, W.J., 2017. Band gap formation and tunability in stretchable serpentine interconnects. J. Appl. Mech. 84, 091007.
Zhang, S., Xia, C., Fang, N., 2011. Broadband acoustic cloak for ultrasound waves. Phys. Rev. Lett. 106, 024301.
Zhu, J., Christensen, J., Jung, J., Martin-Moreno, L., Yin, X., Fok, L., Zhang, X., Garcia-Vidal, F.J., 2011. A holey-structured metamaterial for acoustic deep-subwavelength imaging. Nat. Phys. 7, 52–55.
Zhu, R., Liu, X.N., Hu, G.K., Sun, C.T., Huang, G.L., 2014. Negative refraction of elastic waves at the deep-subwavelength scale in a single-phase metamaterial. Nat. Commun. 5, 5510.
Zigoneanu, L., Popa, B.I., Cummer, S.A., 2014. Three-dimensional broadband omnidirectional acoustic ground cloak. Nat. Mater. 13, 352–355.